Chapter 4

New experimental techniques to retrieve coherence and polarization information from randomness

4.1 Introduction

In the past two decades, there has been a great deal of interest in generating and characterizing beams with non-uniform polarization structures [341–353]. Beams with non-uniform polarization facilitate enhanced control over beam shape, coherence, and polarization at the source plane and in subsequent propagation regions [168,354]. Coherence and polarization play a pivotal role in understanding the essential characteristics of these light beams [168,227]. The two-point correlation either in space or time of the random field characterizes coherence, whereas the single-point correlation between two orthogonal polarization components describes the polarization of light. The coherence and polarization properties of these beams with non-uniform polarization structures can be unified in a common framework, and different field components may exhibit varying coherence properties [168,227,355]. Such fields have been applied in numerous areas, including information photonics [356], coherence shaping [211,286], polarization dynamics [280], depolarization sensing [357], multipurpose sensing [358], super-resolution imaging [359], classification of biological samples [360], microscopy [361,362], optical trapping [363], etc. Given the diverse applications and intrinsic complexity, precise and fast characterization of beams with non-uniform polarization is essential.

To fully characterize the statistical properties of these fields, a unified theory of coherence, treating coherence and polarization in a common framework has been developed [168,227]. Some of these characterization methods include the beam coherence-polarization (BCP) matrix (or cross-spectral density) [168,192], complex degree of coherence [193], generalized Stokes parameters (GSPs) [194], complex degree of mutual polarization [195], degree of polarization in terms of the complex degree of

coherence [197] etc. Among them, the BCP is a 2x2 matrix that involves two-point correlations among same or different polarization components at a pair of points in the beam [192]. The GSPs are also introduced to characterize the vector light fields, and the single-point transformation of the GSPs coincides with the Stokes parameters (SPs) [364,365]. In the realm of a unified theory of coherence, elements of BCP matrix offer a comprehensive statistical characterization of vector light fields [192,193]. Hence, developing fast and efficient experimental techniques for measuring the BCP matrix of vector light fields is of significant practical importance.

A conventional approach for measuring the two-point correlation of a light field relies on first-order intensity in Young's interferometer, wherein two small pinholes enable light from one to interfere with that from the other, and the resulting interference fringe visibility and fringe phase measures the complex correlation function of the light field [198–200]. At the same time, the characterization of BCP matrix of random stationary light beams can be obtained through the analysis of polarization fringes in a Young's experiment [208,218]. In these setups, coherence and polarization information of the stochastic polarized light field is performed using the polarization fringes acquired with suitable retarders and polarizers. Despite its fundamental significance, Young's interferometer faces considerable practical challenges, such as higher measurement time, low light efficiency, stability, etc. Therefore, numerous research efforts have been made to overcome these limitations by developing alternative techniques for experimental measurement of the two-point correlation [202–207,366,367].

Apart from the interferometry based on first-order intensity, interferometry based on the second-order intensity correlation offers an alternate and highly stable experimental configuration to measure the two-point correlation of the light fields [178,285]. These

techniques utilize a common connection between the second-order and first-order correlation of stochastic Gaussian field. However, intensity correlation provides only the modulus of the two-point field correlation while omitting its phase [185]. Correlation holography within the framework of intensity correlation is used to extract the complex coherence function [209]. This methodology is further adapted to facilitate the measurement of the BCP matrix for stationary vector beams [210,221,222]. To filter individual elements of the BCP matrix, a quarter-wave plate (QWP) and a linear polarizer (LP) must be used before the detection of the intensity [210,221,222]. Combinations of the intensity correlation at four different orientations of the QWP are used to recover the complex elements of the BCP matrix. Further, these elements of BCP matrix help to develop imaging methodologies using the vectorial van Cittert Zernike (vCZ) theorem [211]. Moreover, the elements of the BCP matrix have been used to develop some unconventional imaging techniques [213–216].

In another development, Cai et al. have applied a generalized Hanbury Brown Twiss (HBT) approach by introducing two reference fields with controllable phase delay to measure the elements of the BCP matrix [217]. This technique requires four intensity measurements using two charge-coupled devices (CCDs) to evaluate the intensity-intensity cross-correlation of the combined field of references and a vector source. Additionally, they performed four separate intensity measurements of the reference fields and two intensity measurements of the vector source to remove unnecessary background in the intensity-intensity cross-correlation. More recently, a self-referencing holographic technique has been developed for measuring the two-point correlation matrix of vector light beam, requiring eighteen intensity measurements [368].

On the other hand, Visser and co-authors have explored a generalized HBT approach by analyzing polarization correlations [223]. This framework enables the exploration of all possible correlations among the four Stokes parameters (SPs) fluctuations, particularly under Gaussian statistics, where these correlations can be expressed in terms of the two-point field correlations [227]. Leveraging these polarization fluctuations, we have successfully retrieved complex coherence functions and subsequently use it for phase imaging in the correlation holography [238,268,369]. To utilize polarization correlations for the development of statistical characterization and imaging techniques, measurement of SPs is crucial. Traditional SPs measurement requires sequential capture of intensity patterns using mechanically rotated optical elements like a QWP and an LP [27]. Recently, new methods for SPs measurement have been proposed using liquid crystal variable retarders (LCVR), metasurfaces, etc. [128,370–374].

In this chapter, we explored the SPs correlation combined with holography to develop new and alternative techniques for BCP matrix measurement of vector random fields and use it for imaging applications.

4.2 Correlation of Stokes fluctuation to measure BCP matrix

Here, we discuss the use of polarization correlations in statistical characterization of vector random field. The basic principle of the technique is explained below.

Consider a transversely polarized monochromatic light beam with the orthogonal axes *x* and *y* propagating along the *z*-direction. $\boldsymbol{U}(\boldsymbol{\rho},t)=\begin{pmatrix}U_x(\boldsymbol{\rho},t)\\U_y(\boldsymbol{\rho},t)\end{pmatrix}$, represents the complex field at the transverse plane *z*=0, where $U_x(\boldsymbol{\rho}),$ and $U_y(\boldsymbol{\rho})$ are horizontal and vertical

polarization components of the light, respectively, $\boldsymbol{\rho}$ is the spatial position vector at the source plane, and t denotes the time.

The coherent polarized beam propagates through a random scattering media and generates a vector random field at the observation plane located at the far field, as shown in Fig. 4.1.

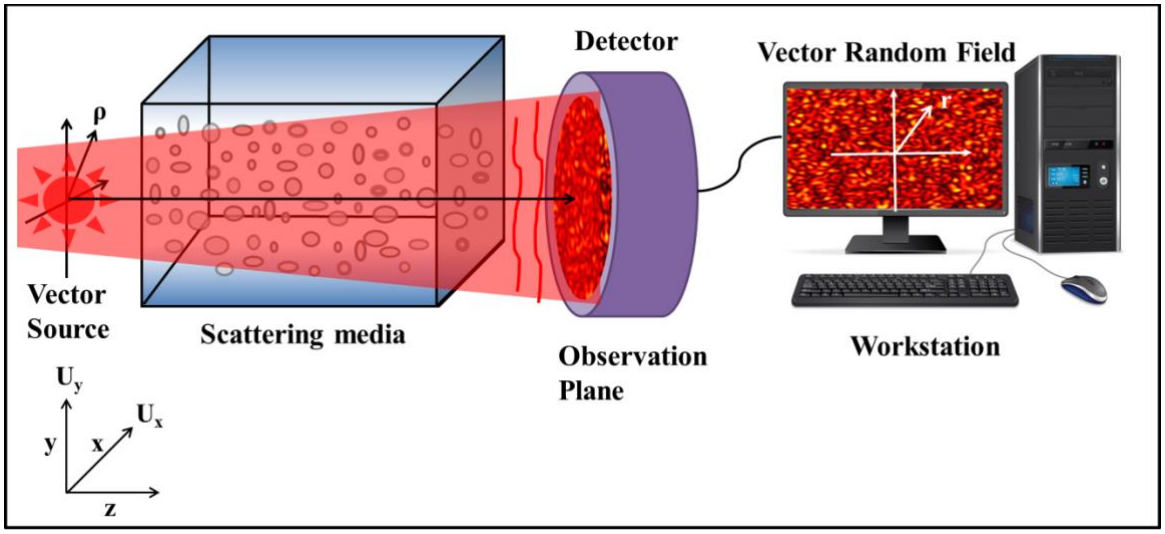

Fig. 4.1 Schematic representation of the generation of vector random field at the far-field by the propagation of vector source through random scattering media.

This field $\boldsymbol{U}(\boldsymbol{r},\mathrm{t})$ is oriented in a direction perpendicular to the overall propagation direction z, and the decomposition of this field into a basis set of transverse unit vectors $(\boldsymbol{e}_p)$ is represented as

$$U_p(\boldsymbol{r},t)=\boldsymbol{U}(\boldsymbol{r},t).\boldsymbol{e}_p \tag{4.1}$$

Here, $\boldsymbol{r}$ is the spatial position vector at the observation plane, and we use a Cartesian basis $p=\{x,y\}$ in which $e_x=\hat{x}$ and $e_y=\hat{y}$.

The instantaneous polarization state of the beam is described by the four SPs as

$$S_m(\boldsymbol{r},t)=\boldsymbol{U}^{\dagger}(\boldsymbol{r},t)\boldsymbol{\sigma}^m\boldsymbol{U}(\boldsymbol{r},t),\qquad (m=0,1,2,3), \tag{4.2}$$

where, $\boldsymbol{\sigma}$ represents the Pauli spin matrices and $\dagger$ denotes Hermitian conjugate.

The fluctuations of SPs around their average value are evaluated as

$$\Delta S_m(\boldsymbol{r},t) = S_m(\boldsymbol{r},t) - \langle S_m(\boldsymbol{r},t)\rangle, \tag{4.3}$$

where, $\langle S_m(\boldsymbol{r},t)\rangle$ denotes its average value. For the sake of brevity, we have ignored time *t* in the coming sections.

All possible pairs of the two-point correlations between the various fluctuations of SPs can be described using a 4 × 4 matrix with elements as

$$C_{mn}(\boldsymbol{r_1},\boldsymbol{r_2}) = \langle \Delta S_m(\boldsymbol{r_1})\Delta S_n(\boldsymbol{r_2})\rangle, \quad (m,n=0,1,2,3),$$

$$= \langle S_m(\boldsymbol{r_1})S_n(\boldsymbol{r_2})\rangle - \langle S_m(\boldsymbol{r_1})\rangle\langle S_n(\boldsymbol{r_2})\rangle \tag{4.4}$$

where, $\langle\ \rangle$ represents ensemble average. Assuming stationarity and ergodicity at the observation plane, the ensemble average can be replaced with either the time average or space average.

Substituting Eq. (4.2) into Eq. (4.4) results into,

$$C_{mn}(\boldsymbol{r_1},\boldsymbol{r_2}) = \boldsymbol{\sigma}^m\boldsymbol{\sigma}^n\langle \boldsymbol{U}^\dagger(\boldsymbol{r}_1)\boldsymbol{U}(\boldsymbol{r}_1)\boldsymbol{U}^\dagger(\boldsymbol{r}_2)\boldsymbol{U}(\boldsymbol{r}_2)\rangle - \boldsymbol{\sigma}^m\langle \boldsymbol{U}^\dagger(\boldsymbol{r}_1)\boldsymbol{U}(\boldsymbol{r}_1)\rangle\boldsymbol{\sigma}^n\langle \boldsymbol{U}^\dagger(\boldsymbol{r}_2)\boldsymbol{U}(\boldsymbol{r}_2)\rangle. \tag{4.5}$$

For the Gaussian random fields, the second-order intensity correlation in Eq. (4.5) is expressed as the sum of products of two-point field correlations. Therefore, elements of the matrix are expressed as

$$C_{mn}(\boldsymbol{r_1},\boldsymbol{r_2}) = \boldsymbol{\sigma}^m\boldsymbol{\sigma}^n\left[\langle \boldsymbol{U}^\dagger(\boldsymbol{r}_1)\boldsymbol{U}(\boldsymbol{r}_1)\rangle\langle \boldsymbol{U}^\dagger(\boldsymbol{r}_2)\boldsymbol{U}(\boldsymbol{r}_2)\rangle + \langle \boldsymbol{U}^\dagger(\boldsymbol{r}_1)\boldsymbol{U}(\boldsymbol{r}_2)\rangle\langle \boldsymbol{U}^\dagger(\boldsymbol{r}_2)\boldsymbol{U}(\boldsymbol{r}_1)\rangle\right]$$
$$-\boldsymbol{\sigma}^m\langle \boldsymbol{U}^\dagger(\boldsymbol{r}_1)\boldsymbol{U}(\boldsymbol{r}_1)\rangle\boldsymbol{\sigma}^n\langle \boldsymbol{U}^\dagger(\boldsymbol{r}_2)\boldsymbol{U}(\boldsymbol{r}_2)\rangle,$$

$$= tr\left[\boldsymbol{\sigma}^m\boldsymbol{W}^\dagger(\boldsymbol{r_1},\boldsymbol{r_2})\boldsymbol{\sigma}^n\boldsymbol{W}(\boldsymbol{r_1},\boldsymbol{r_2})\right], \tag{4.6}$$

where, '*tr*' stands for trace.

The statistical property of a stochastic field can be characterized by the BCP matrix, which is defined as [192]

$$\boldsymbol{W}(\boldsymbol{r_1},\boldsymbol{r_2}) = \begin{pmatrix} W_{pp}(\boldsymbol{r_1},\boldsymbol{r_2}) & W_{pq}(\boldsymbol{r_1},\boldsymbol{r_2}) \\ W_{qp}(\boldsymbol{r_1},\boldsymbol{r_2}) & W_{qq}(\boldsymbol{r_1},\boldsymbol{r_2}) \end{pmatrix}, \tag{4.7}$$

Elements of the BCP matrix are expressed as $W_{pq}(\boldsymbol{r_1},\boldsymbol{r_2}) = \left\langle U_p^*(\boldsymbol{r_1}) U_q(\boldsymbol{r_2}) \right\rangle$, where $(p,q = x,y)$, and star * denotes the complex conjugate.

The Stokes correlation matrix, constructed using SPs fluctuation correlation as described in Eq. (4.4), is expressed as

$$\boldsymbol{C}(\boldsymbol{r_1},\boldsymbol{r_2}) = \begin{pmatrix} C_{00}(\boldsymbol{r_1},\boldsymbol{r_2}) & C_{01}(\boldsymbol{r_1},\boldsymbol{r_2}) & C_{02}(\boldsymbol{r_1},\boldsymbol{r_2}) & C_{03}(\boldsymbol{r_1},\boldsymbol{r_2}) \\ C_{10}(\boldsymbol{r_1},\boldsymbol{r_2}) & C_{11}(\boldsymbol{r_1},\boldsymbol{r_2}) & C_{12}(\boldsymbol{r_1},\boldsymbol{r_2}) & C_{13}(\boldsymbol{r_1},\boldsymbol{r_2}) \\ C_{20}(\boldsymbol{r_1},\boldsymbol{r_2}) & C_{21}(\boldsymbol{r_1},\boldsymbol{r_2}) & C_{22}(\boldsymbol{r_1},\boldsymbol{r_2}) & C_{23}(\boldsymbol{r_1},\boldsymbol{r_2}) \\ C_{30}(\boldsymbol{r_1},\boldsymbol{r_2}) & C_{31}(\boldsymbol{r_1},\boldsymbol{r_2}) & C_{32}(\boldsymbol{r_1},\boldsymbol{r_2}) & C_{33}(\boldsymbol{r_1},\boldsymbol{r_2}) \end{pmatrix}, \tag{4.8}$$

A first diagonal element of the matrix, i.e., $C_{00}(\boldsymbol{r_1},\boldsymbol{r_2})$ is expressed as

$$\mathrm{C}_{00}(\boldsymbol{r_1},\boldsymbol{r_2}) = tr\left[\boldsymbol{\sigma}^0 \boldsymbol{W}^\dagger(\boldsymbol{r_1},\boldsymbol{r_2}) \boldsymbol{\sigma}^0 \boldsymbol{W}(\boldsymbol{r_1},\boldsymbol{r_2})\right],$$

$$= tr\left[\begin{pmatrix} 1 & 0 \\ 0 & 1 \end{pmatrix}\begin{pmatrix} W_{xx}^*(\boldsymbol{r_1},\boldsymbol{r_2}) & W_{yx}^*(\boldsymbol{r_1},\boldsymbol{r_2}) \\ W_{xy}^*(\boldsymbol{r_1},\boldsymbol{r_2}) & W_{yy}^*(\boldsymbol{r_1},\boldsymbol{r_2}) \end{pmatrix}\begin{pmatrix} 1 & 0 \\ 0 & 1 \end{pmatrix}\begin{pmatrix} W_{xx}(\boldsymbol{r_1},\boldsymbol{r_2}) & W_{xy}(\boldsymbol{r_1},\boldsymbol{r_2}) \\ W_{yx}(\boldsymbol{r_1},\boldsymbol{r_2}) & W_{yy}(\boldsymbol{r_1},\boldsymbol{r_2}) \end{pmatrix}\right],$$

$$= \left|W_{xx}(\boldsymbol{r_1},\boldsymbol{r_2})\right|^2 + \left|W_{xy}(\boldsymbol{r_1},\boldsymbol{r_2})\right|^2 + \left|W_{yx}(\boldsymbol{r_1},\boldsymbol{r_2})\right|^2 + \left|W_{yy}(\boldsymbol{r_1},\boldsymbol{r_2})\right|^2, \tag{4.9}$$

Similarly, the other fifteen elements of the Stokes correlation matrix are expressed as

$$C_{01}(\boldsymbol{r_1},\boldsymbol{r_2}) = \left|W_{xx}(\boldsymbol{r_1},\boldsymbol{r_2})\right|^2 - \left|W_{xy}(\boldsymbol{r_1},\boldsymbol{r_2})\right|^2 + \left|W_{yx}(\boldsymbol{r_1},\boldsymbol{r_2})\right|^2 - \left|W_{yy}(\boldsymbol{r_1},\boldsymbol{r_2})\right|^2, \tag{4.10}$$

$$C_{02}(\boldsymbol{r_1},\boldsymbol{r_2}) = 2\,\mathrm{Re}\left[W_{xx}(\boldsymbol{r_1},\boldsymbol{r_2}) W_{xy}^*(\boldsymbol{r_1},\boldsymbol{r_2}) + W_{yy}(\boldsymbol{r_1},\boldsymbol{r_2}) W_{yx}^*(\boldsymbol{r_1},\boldsymbol{r_2})\right], \tag{4.11}$$

$$C_{03}(\boldsymbol{r_1},\boldsymbol{r_2}) = 2\,Im\left[W_{yy}(\boldsymbol{r_1},\boldsymbol{r_2}) W_{yx}^*(\boldsymbol{r_1},\boldsymbol{r_2}) - W_{xx}(\boldsymbol{r_1},\boldsymbol{r_2}) W_{xy}^*(\boldsymbol{r_1},\boldsymbol{r_2})\right], \tag{4.12}$$

$$C_{10}(\boldsymbol{r_1},\boldsymbol{r_2}) = \left|W_{xx}(\boldsymbol{r_1},\boldsymbol{r_2})\right|^2 + \left|W_{xy}(\boldsymbol{r_1},\boldsymbol{r_2})\right|^2 - \left|W_{yx}(\boldsymbol{r_1},\boldsymbol{r_2})\right|^2 - \left|W_{yy}(\boldsymbol{r_1},\boldsymbol{r_2})\right|^2, \tag{4.13}$$

$$C_{11}(\boldsymbol{r_1},\boldsymbol{r_2}) = \left|W_{xx}(\boldsymbol{r_1},\boldsymbol{r_2})\right|^2 - \left|W_{xy}(\boldsymbol{r_1},\boldsymbol{r_2})\right|^2 - \left|W_{yx}(\boldsymbol{r_1},\boldsymbol{r_2})\right|^2 + \left|W_{yy}(\boldsymbol{r_1},\boldsymbol{r_2})\right|^2, \tag{4.14}$$

$$C_{12}(\boldsymbol{r_1},\boldsymbol{r_2}) = 2\,\mathrm{Re}\left[W_{xx}(\boldsymbol{r_1},\boldsymbol{r_2})W_{xy}^{*}(\boldsymbol{r_1},\boldsymbol{r_2}) - W_{yy}(\boldsymbol{r_1},\boldsymbol{r_2})W_{yx}^{*}(\boldsymbol{r_1},\boldsymbol{r_2})\right], \tag{4.15}$$

$$C_{13}(\boldsymbol{r_1},\boldsymbol{r_2}) = 2Im\left[W_{xy}(\boldsymbol{r_1},\boldsymbol{r_2})W_{xx}^{*}(\boldsymbol{r_1},\boldsymbol{r_2}) + W_{yx}(\boldsymbol{r_1},\boldsymbol{r_2})W_{yy}^{*}(\boldsymbol{r_1},\boldsymbol{r_2})\right], \tag{4.16}$$

$$C_{20}(\boldsymbol{r_1},\boldsymbol{r_2}) = 2\,\mathrm{Re}\left[W_{xx}(\boldsymbol{r_1},\boldsymbol{r_2})W_{yx}^{*}(\boldsymbol{r_1},\boldsymbol{r_2}) + W_{yy}(\boldsymbol{r_1},\boldsymbol{r_2})W_{xy}^{*}(\boldsymbol{r_1},\boldsymbol{r_2})\right], \tag{4.17}$$

$$C_{21}(\boldsymbol{r_1},\boldsymbol{r_2}) = 2\,\mathrm{Re}\left[W_{xx}(\boldsymbol{r_1},\boldsymbol{r_2})W_{yx}^{*}(\boldsymbol{r_1},\boldsymbol{r_2}) - W_{yy}(\boldsymbol{r_1},\boldsymbol{r_2})W_{xy}^{*}(\boldsymbol{r_1},\boldsymbol{r_2})\right], \tag{4.18}$$

$$C_{22}(\boldsymbol{r_1},\boldsymbol{r_2}) = 2\,\mathrm{Re}\left[W_{xx}(\boldsymbol{r_1},\boldsymbol{r_2})W_{yy}^{*}(\boldsymbol{r_1},\boldsymbol{r_2}) + W_{xy}(\boldsymbol{r_1},\boldsymbol{r_2})W_{yx}^{*}(\boldsymbol{r_1},\boldsymbol{r_2})\right], \tag{4.19}$$

$$C_{23}(\boldsymbol{r_1},\boldsymbol{r_2}) = 2Im\left[W_{xy}(\boldsymbol{r_1},\boldsymbol{r_2})W_{yx}^{*}(\boldsymbol{r_1},\boldsymbol{r_2}) + W_{yy}(\boldsymbol{r_1},\boldsymbol{r_2})W_{xx}^{*}(\boldsymbol{r_1},\boldsymbol{r_2})\right], \tag{4.20}$$

$$C_{30}(\mathbf{r_1},\mathbf{r_2}) = 2Im\left[W_{xx}(\mathbf{r_1},\mathbf{r_2})W_{yx}^{*}(\mathbf{r_1},\mathbf{r_2}) - W_{yy}(\mathbf{r_1},\mathbf{r_2})W_{xy}^{*}(\mathbf{r_1},\mathbf{r_2})\right], \tag{4.21}$$

$$C_{31}(\boldsymbol{r_1},\boldsymbol{r_2}) = 2Im\left[W_{xx}(\boldsymbol{r_1},\boldsymbol{r_2})W_{yx}^{*}(\boldsymbol{r_1},\boldsymbol{r_2}) + W_{yy}(\boldsymbol{r_1},\boldsymbol{r_2})W_{xy}^{*}(\boldsymbol{r_1},\boldsymbol{r_2})\right], \tag{4.22}$$

$$C_{32}(\boldsymbol{r_1},\boldsymbol{r_2}) = 2\,\mathrm{Im}\left[W_{xy}(\boldsymbol{r_1},\boldsymbol{r_2})W_{yx}^{*}(\boldsymbol{r_1},\boldsymbol{r_2}) + W_{xx}(\boldsymbol{r_1},\boldsymbol{r_2})W_{yy}^{*}(\boldsymbol{r_1},\boldsymbol{r_2})\right], \tag{4.23}$$

$$C_{33}(\boldsymbol{r_1},\boldsymbol{r_2}) = 2\,\mathrm{Re}\left[W_{xx}(\boldsymbol{r_1},\boldsymbol{r_2})W_{yy}^{*}(\boldsymbol{r_1},\boldsymbol{r_2}) - W_{xy}(\boldsymbol{r_1},\boldsymbol{r_2})W_{yx}^{*}(\boldsymbol{r_1},\boldsymbol{r_2})\right], \tag{4.24}$$

The different combinations of the complex Stokes correlation matrix elements are now utilized to develop and design BCP matrix measurement techniques.

In this chapter, out of the 16 elements in Stokes correlation matrix Eq. (4.8), we utilize only 4 elements $C_{00}(\boldsymbol{r_1},\boldsymbol{r_2}), C_{01}(\boldsymbol{r_1},\boldsymbol{r_2}), C_{10}(\boldsymbol{r_1},\boldsymbol{r_2}), C_{11}(\boldsymbol{r_1},\boldsymbol{r_2})$ to develop a new theoretical framework to measure the BCP matrix as represented in Eq. (4.7).

Different combinations of these 4 elements $C_{00}(\boldsymbol{r_1},\boldsymbol{r_2}), C_{01}(\boldsymbol{r_1},\boldsymbol{r_2}), C_{10}(\boldsymbol{r_1},\boldsymbol{r_2}), C_{11}(\boldsymbol{r_1},\boldsymbol{r_2})$ as shown in Eqs. (4.9, 4.10, 4.13, 4.14) are utilized to extract all four elements of the BCP matrix as follows

$$\frac{1}{4}\left[\left(C_{00}(\boldsymbol{r_1},\boldsymbol{r_2}) + C_{11}(\boldsymbol{r_1},\boldsymbol{r_2})\right) + \left(C_{10}(\boldsymbol{r_1},\boldsymbol{r_2}) + C_{01}(\boldsymbol{r_1},\boldsymbol{r_2})\right)\right] = \left|W_{xx}(\boldsymbol{r_1},\boldsymbol{r_2})\right|^2, \tag{4.25}$$

$$\frac{1}{4}\left[\left(C_{00}(\boldsymbol{r_1},\boldsymbol{r_2})+C_{11}(\boldsymbol{r_1},\boldsymbol{r_2})\right)-\left(C_{10}(\boldsymbol{r_1},\boldsymbol{r_2})+C_{01}(\boldsymbol{r_1},\boldsymbol{r_2})\right)\right]=\left|W_{yy}(\boldsymbol{r_1},\boldsymbol{r_2})\right|^2, \tag{4.26}$$

$$\frac{1}{4}\left[\left(C_{00}(\boldsymbol{r_1},\boldsymbol{r_2})-C_{11}(\boldsymbol{r_1},\boldsymbol{r_2})\right)+\left(C_{10}(\boldsymbol{r_1},\boldsymbol{r_2})-C_{01}(\boldsymbol{r_1},\boldsymbol{r_2})\right)\right]=\left|W_{xy}(\boldsymbol{r_1},\boldsymbol{r_2})\right|^2, \tag{4.27}$$

$$\frac{1}{4}\left[\left(C_{00}(\boldsymbol{r_1},\boldsymbol{r_2})-C_{11}(\boldsymbol{r_1},\boldsymbol{r_2})\right)-\left(C_{10}(\boldsymbol{r_1},\boldsymbol{r_2})-C_{01}(\boldsymbol{r_1},\boldsymbol{r_2})\right)\right]=\left|W_{yx}(\boldsymbol{r_1},\boldsymbol{r_2})\right|^2, \tag{4.28}$$

These four elements of the BCP matrix are generally a complex quantity. However, the correlation of fluctuations of SPs provides the squared modulus of the complex coherence function, and phase is lost.

Here, we adopted a holographic approach combined with the second-order correlation of the SPs to extract complex elements of the BCP matrix.

Let us consider the stochastic random field as a superposition of two coherent random fields as follows

$$U_p(\boldsymbol{r})=U_p^1(\boldsymbol{r})+U_p^2(\boldsymbol{r}), \tag{4.29}$$

where, $U_p^1(\boldsymbol{r})$ and $U_p^2(\boldsymbol{r})$ are to-be-analyzed vector source and known reference fields, respectively.

Therefore, the two-point correlation of the field components is represented as

$$\left\langle U_p^*(\boldsymbol{r_1})U_q(\boldsymbol{r_2})\right\rangle=\left\langle U_p^{1*}(\boldsymbol{r_1})U_q^1(\boldsymbol{r_2})\right\rangle+\left\langle U_p^{2*}(\boldsymbol{r_1})U_q^2(\boldsymbol{r_2})\right\rangle \tag{4.30}$$

as $\left\langle U_p^{1*}(\boldsymbol{r_1})U_q^2(\boldsymbol{r_2})\right\rangle\approx 0$, due to considering two statistically independent to-be-analyzed and reference fields in Eq. (4.29).

Upon substituting Eq. (4.30) into Eqs. (4.6, 4.9, 4.10, 4.13, 4.14), the right-hand side of Eqs. (4.25)-(4.28) transform as

$$\begin{aligned}\left|W_{pq}(\boldsymbol{r_1},\boldsymbol{r_2})\right|^2&=\left|W_{pq}^1(\boldsymbol{r_1},\boldsymbol{r_2})+W_{pq}^2(\boldsymbol{r_1},\boldsymbol{r_2})\right|^2,\\&=\left|W_{pq}^1(\boldsymbol{r_1},\boldsymbol{r_2})\right|^2+\left|W_{pq}^2(\boldsymbol{r_1},\boldsymbol{r_2})\right|^2+W_{pq}^1(\boldsymbol{r_1},\boldsymbol{r_2})W_{pq}^{2\,*}(\boldsymbol{r_1},\boldsymbol{r_2})+W_{pq}^{1\,*}(\boldsymbol{r_1},\boldsymbol{r_2})W_{pq}^2(\boldsymbol{r_1},\boldsymbol{r_2})\end{aligned} \tag{4.31}$$

where, $W_{pq}^{1}(\boldsymbol{r_1},\boldsymbol{r_2}) = \left\langle U_p^{1*}(\boldsymbol{r_1}) U_q^{1}(\boldsymbol{r_2}) \right\rangle$ and $W_{pq}^{2}(\boldsymbol{r_1},\boldsymbol{r_2}) = \left\langle U_p^{2*}(\boldsymbol{r_1}) U_q^{2}(\boldsymbol{r_2}) \right\rangle$ represents the elements of the BCP matrix for the to-be-analyzed and a reference field, respectively.

Eq. (4.31) demonstrates the presence of fringes in certain combinations of the Stokes correlation as described in Eqs. (4.25)-(4.28). The reference coherence function $W_{pq}^{2}(\boldsymbol{r_1},\boldsymbol{r_2})$ covers the support of the vector source's coherence function $W_{pq}^{1}(\boldsymbol{r_1},\boldsymbol{r_2})$ to record the fringes in the Stokes correlation. Fourier processing of Eq. (4.31) helps to recover the complex elements of the BCP matrix, $W_{pq}^{1}(\boldsymbol{r_1},\boldsymbol{r_2})$. In the Fourier processing, a Fourier transform of Eq. (4.31) consists of four terms as follows

$$FT\left\{\left|W_{pq}(\boldsymbol{r_1},\boldsymbol{r_2})\right|^2\right\} = FT\left\{W_{pq}^{1}(\boldsymbol{r_1},\boldsymbol{r_2})\right\} \otimes FT\left\{W_{pq}^{1\,*}(\boldsymbol{r_1},\boldsymbol{r_2})\right\} + FT\left\{W_{pq}^{2}(\boldsymbol{r_1},\boldsymbol{r_2})\right\} \otimes FT\left\{W_{pq}^{2\,*}(\boldsymbol{r_1},\boldsymbol{r_2})\right\}$$
$$+FT\left\{W_{pq}^{1}(\boldsymbol{r_1},\boldsymbol{r_2})\right\} \otimes FT\left\{W_{pq}^{2\,*}(\boldsymbol{r_1},\boldsymbol{r_2})\right\} + FT\left\{W_{pq}^{2}(\boldsymbol{r_1},\boldsymbol{r_2})\right\} \otimes FT\left\{W_{pq}^{1\,*}(\boldsymbol{r_1},\boldsymbol{r_2})\right\}. \tag{4.32}$$

where, $\otimes$ and FT{.} represent two-dimensional (2D) convolution and Fourier transform, respectively. The first two terms on the right-hand side of Eq. (4.32) represent the central DC, which is digitally suppressed. The third and fourth terms containing the vector source information can be separated from central DC by properly introducing the reference field and further helping to reconstruct the desired elements of the BCP matrix.

Hence, our developed theoretical basis requires two-point correlations of only two SPs, S_0 and S_1, to evaluate the BCP matrix of the vector random field as discussed above. Experimental measurements of these two SPs are facilitated in two ways: (i) inserting a linear polarizer before the detector and capturing two shots of intensities to capture the orthogonally polarized intensity patterns, or (ii) measuring the intensities or orthogonally polarized components simultaneously in a single-shot using two channels.

Additionally, in practical application scenarios, the random scattering media encountered by the vector field can be implemented in various forms, including static environments like static scattering walls and dynamic like fog or atmospheric turbulence. Propagation of vector source through static and dynamic environment conditions generates vector random fields at the far-field, which exhibits spatially and temporally fluctuating intensity patterns, respectively. Therefore, the statistical characterization of both spatially and temporally fluctuating vector fields is of utmost importance.

This chapter explores static and dynamic vector fields and designs new experimental techniques for the BCP matrix measurement of vector random fields. Measurement of the BCP matrix is demonstrated in three different experimental scenarios, providing a comprehensive framework for analyzing vector random fields. A list of the three experimental scenarios is provided below to aid understanding.

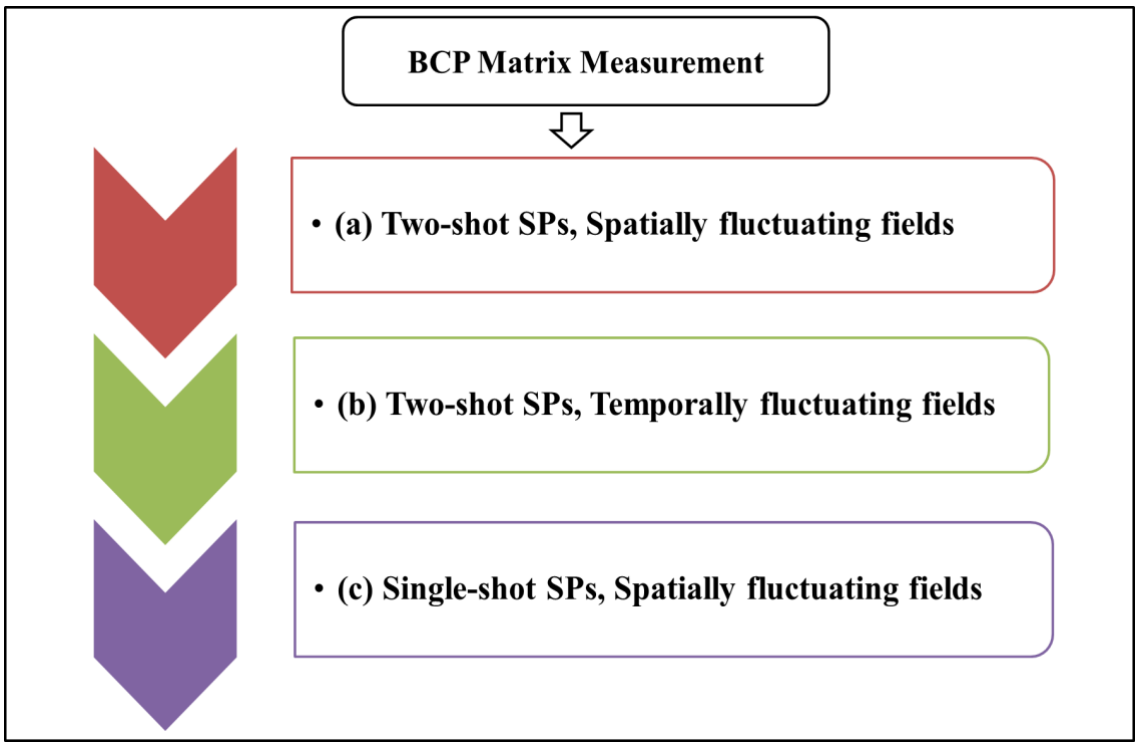

These three experimental techniques are discussed below.

4.3 Two-shot SPs to measure BCP matrix

To implement the SP fluctuations combined with a holographic approach for the measurement of the BCP matrix, an appropriate interferometer is required to make the interference of the to-be-analyzed vector source and a known reference. For this purpose, we have designed a folded interferometer to effectively make an interference of the coherence waves coming from to-be-analyzed vector source and reference. This interferometer utilizes a cube beam splitter (BS) to create a folded wavefront replica. These two replicas are used as an object and reference arm for our holographic approach. Hence, the developed folded interferometer eliminates the need for a separate reference arm for complex correlation measurement through a holographic approach. Importantly, our technique relies on beam reflections rather than diffraction through the Young double-slit mask [198], maximizing light efficiency. The objective of our technique is to measure two-point correlations of the spatially fluctuating vector fields, which may be complex, i.e., amplitude and argument. The desired SPs, namely S_0 and S_1 of the superposed spatially fluctuating fields of the to-be-analyzed vector source and a reference, are recorded, and correlations of the fluctuations of these two SPs are used to determine all four elements of the BCP matrix. The advantage of this experimental design lies in its ability to measure all four elements of the BCP matrix by a simple, compact, folded interferometry geometry. Compared to the other techniques [210,217,221,368], the proposed method can measure the BCP matrix from two shots of intensities.

4.3.1 Experiment

To illustrate the feasibility of our proposed technique, we present an experimental design as shown in Fig. 4.2. A spatially filtered and collimated He-Ne laser (Thorlabs, HNL150L) at 632.8 nm is converted to a 45° linearly polarized beam by a half-wave plate

(HWP). The beam impinges onto a phase-only spatial light modulator (SLM) with a resolution of 1920 × 1080 and a pixel pitch of 8 μm (Pluto from Holoeye). Consequently, the information is loaded into the horizontal polarization component of the beam, and the vertical polarization component remains intact.

The beam coming from the SLM propagates towards our specially designed folded interferometer. With its elegant utilization of a cube BS, this interferometer showcases a compact approach to create a folded wavefront replica. One of the two emerging replicas, denoted by arm 1, carries the complex information encoded by the SLM, whereas arm 2 acts as a reference to realize a compact folded interferometer. The replica of arm 2 is focused at the center of the pinhole aperture (PA) with the help of lens L1 of focal length f=100 mm, which generates a reference point source. The BS is oriented so that the two emerging replicas fall on two separate spatial regions of the ground glass (GG). This configuration eliminates the need for an additional reference arm for complex correlation measurement. The randomly scattered field, composed of coherent superposition of the coherent random fields from arms 1 and 2, is Fourier transformed by a lens L2 (f=200 mm) and recorded by a CCD at the Fourier plane. The generated random field at the CCD plane follows the Gaussian statistics.

An instantaneous complex field at the CCD plane is represented as

$$U_p(\boldsymbol{r}) = \int U_p^1(\boldsymbol{\rho}) \exp\left(-i\frac{2\pi}{\lambda f}\boldsymbol{r}.\boldsymbol{\rho}\right) d^2\boldsymbol{\rho} + \int U_p^2(\boldsymbol{\rho}) \exp\left(-i\frac{2\pi}{\lambda f}\boldsymbol{r}.\boldsymbol{\rho}\right) d^2\boldsymbol{\rho} \tag{4.33}$$

Hence, elements of the BCP matrix at the CCD plane are expressed as

$$W_{pq}(\boldsymbol{r_1}, \boldsymbol{r_2}) = \left\langle U_p^{1*}(\boldsymbol{r_1}) U_q^1(\boldsymbol{r}_2) \right\rangle + \left\langle U_p^{2*}(\boldsymbol{r_1}) U_q^2(\boldsymbol{r}_2) \right\rangle \tag{4.34}$$

where, $\left\langle U_p^{1*}(\boldsymbol{r_1})U_q^2(\boldsymbol{r_2})\right\rangle \approx 0$, due to the consideration of two statistically independent fields emerging from the GG.

A spatial stationarity at the Fourier geometry detector plane permits the ensemble average's replacement by a spatial average [159]**.** Considering $\boldsymbol{r_1} = \boldsymbol{r}, \boldsymbol{r_2} = \boldsymbol{r} + \Delta\boldsymbol{r}$ and the use of spatial averaging at the Fourier plane, the two-point correlation function is expressed as

$$W_{pq}(\boldsymbol{r}, \boldsymbol{r}+\Delta\boldsymbol{r}) = \int\left\{\iint U_p^{1*}(\boldsymbol{\rho_1})U_q^1(\boldsymbol{\rho_2})\exp\left(-i\frac{2\pi}{\lambda f}\left[(\boldsymbol{r}+\Delta\boldsymbol{r})\boldsymbol{.\rho_2} - \boldsymbol{r.\rho}_1\right]\right)d^2\boldsymbol{\rho}_1 d^2\boldsymbol{\rho}_2\right\}d^2\boldsymbol{r}$$
$$+\int\left\{\iint U_p^{2*}(\boldsymbol{\rho_1})U_q^2(\boldsymbol{\rho_2})\exp\left(-i\frac{2\pi}{\lambda f}\left[(\boldsymbol{r}+\Delta\boldsymbol{r})\boldsymbol{.\rho_2} - \boldsymbol{r.\rho}_1\right]\right)d^2\boldsymbol{\rho}_1 d^2\boldsymbol{\rho}_2\right\}d^2\boldsymbol{r} \tag{4.35}$$

In Eq. (4.35), the integration taken over the Fourier plane for spatial averaging results in a delta function, i.e.

$$\int\exp\left(-i\frac{2\pi}{\lambda f}\left[\boldsymbol{r}.(\boldsymbol{\rho_2}-\boldsymbol{\rho}_1)\right]\right)d^2\boldsymbol{r} \propto \delta(\boldsymbol{\rho_2}-\boldsymbol{\rho}_1) \tag{4.36}$$

For $\boldsymbol{\rho_1} = \boldsymbol{\rho}_2 = \boldsymbol{\rho}$, this relation transforms to

$$W_{pq}(\Delta\boldsymbol{r}) = \int I_{pq}(\boldsymbol{\rho})\exp\left(-i\frac{2\pi}{\lambda f}\Delta\boldsymbol{r.\rho}\right)d^2\boldsymbol{\rho}, \tag{4.37}$$

where, $\mathrm{I}_{pq}(\boldsymbol{\rho}) = \mathrm{I}_{pq}^1(\boldsymbol{\rho}) + \mathrm{I}_{pq}^2(\boldsymbol{\rho})$ represents the source at the GG plane as a composition of two independent sources.

Thus, the elements of the BCP matrices of the field to-be-analyzed and a reference are represented as

$$W_{pq}^{1}(\Delta \boldsymbol{r}) = \int I_{pq}^{1}(\boldsymbol{\rho}) \exp\left(-i \frac{2\pi}{\lambda f} \Delta \boldsymbol{r}.\boldsymbol{\rho} \right) d^2\boldsymbol{\rho}, \tag{4.38}$$

$$W_{pq}^{2}(\Delta \boldsymbol{r}) = \int I_{pq}^{2}(\boldsymbol{\rho}) \exp\left(-i \frac{2\pi}{\lambda f} \Delta \boldsymbol{r}.\boldsymbol{\rho} \right) d^2\boldsymbol{\rho}, \tag{4.39}$$

For an off-axis reference point, the elements of the reference coherence matrix are expressed as

$$W_{pq}^{2}(\Delta \boldsymbol{r}) = \int circ\left(\frac{\boldsymbol{\rho} - \boldsymbol{\rho_0}}{a_0} \right) \exp\left(-i \frac{2\pi}{\lambda f} \Delta \boldsymbol{r}.\boldsymbol{\rho} \right) d^2\boldsymbol{\rho}, \tag{4.40}$$

where, $\boldsymbol{\rho_0}$ is the off-axis location of the reference point at the GG plane while a_0 represents the aperture size at the GG plane. The aperture size a_0 is very small to generate a uniform reference coherence $W_{pq}^{2}(\Delta \boldsymbol{r})$ to cover the support of $W_{pq}^{1}(\Delta \boldsymbol{r})$ as desired in Eq. (4.31).

To experimentally measure all four elements of the BCP matrix, we inserted a LP before the CCD and record the orthogonal polarization components of the vector random field to measure the desired SPs. These two SPs are calculated as [119]

$$S_0(\boldsymbol{r}) = I(\boldsymbol{r}, 0^0) + I(\boldsymbol{r}, 90^0), \tag{4.41}$$

$$S_1(\boldsymbol{r}) = I(\boldsymbol{r}, 0^0) - I(\boldsymbol{r}, 90^0), \tag{4.42}$$

where, $I(\boldsymbol{r}, \theta)$ represent the instantaneous intensity at the camera plane and θ refers to the angle of LP.

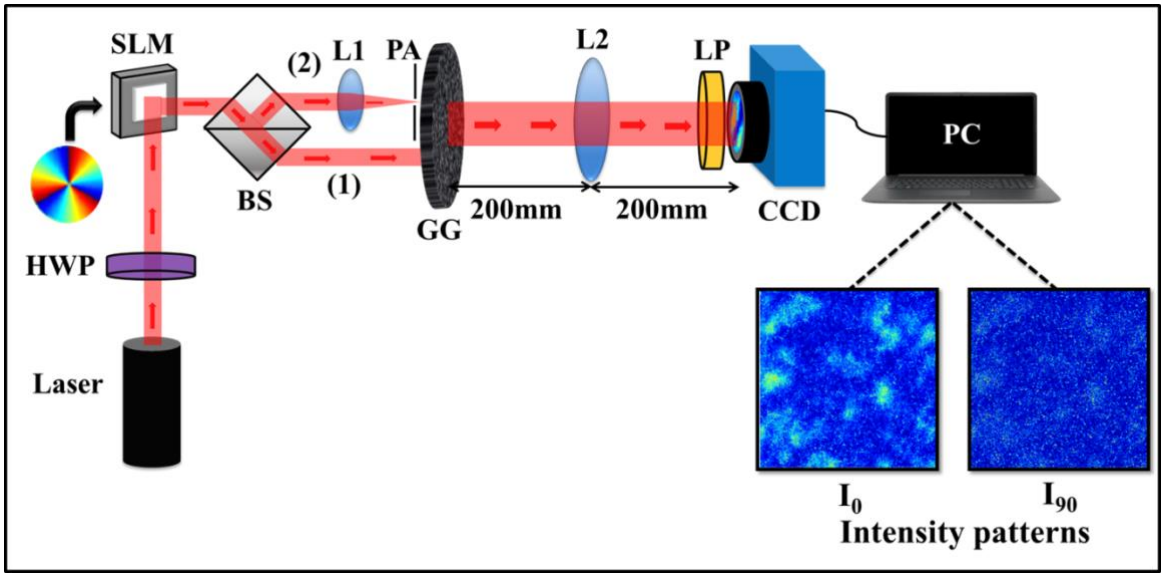

Fig. 4.2 Experimental implementation of the proposed technique. BS: Beam splitter, GG: Ground Glass, L1, L2: Lenses, PA: Pinhole Aperture, LP: Linear polarizer, CCD: Charge-coupled device, PC: Personal Computer. Labels (1) and (2) denote arm 1 and arm 2, respectively.

The correlation between fluctuations of SPs is digitally evaluated from the experimentally measured SPs using spatial averaging to replace the ensemble averaging for Gaussian statistics. This process provides $C_{00}(\Delta \boldsymbol{r}), C_{01}(\Delta \boldsymbol{r}), C_{10}(\Delta \boldsymbol{r}), C_{11}(\Delta \boldsymbol{r})$ from the experimental measured SPs and complex elements of the BCP matrix are retrieved as explained in Eqs. (4.4-4.31).

4.3.2 Experimental results and discussions

To check the performance of our technique, we have experimentally synthesized a vector source by loading a vortex structure in the *x*-polarization component of the incident 45^0 linearly polarized beam, and the *y*-polarization component consists of a plane wave, i.e., $U_x(\boldsymbol{\rho}) = exp(il\varphi), U_y(\boldsymbol{\rho}) = 1$ where φ is the azimuthal phase, and l is the topological charge.

Experimentally recorded intensity patterns of the orthogonal polarization components of the vector random field, as shown in Fig. 4.2, are used to evaluate $S_0(\boldsymbol{r}), S_1(\boldsymbol{r})$ from Eqs. (4.41), and (4.42). This process is sketched in Fig. 4.3(a). From the experimentally measured SPs, digital evaluations of correlations of fluctuations of the SPs are acquired by spatial averaging. This process is executed by taking SPs as a matrix with spatial varying points, represented as, $S_m^k(\boldsymbol{r})$, where m = 0, 1, denotes the first two SPs involved in the estimation of polarization correlation, and $\boldsymbol{r} = (x, y)$ is spatial pixel coordinate. The two-point correlation of fluctuations of SPs for the different realizations of the window of SPs is represented as $\sum_{k=1}^{K}\left[\Delta S_m^k(x,y)\Delta S_m^k(0,0)\right]/K$. Here, K represents the total number of different realizations of the matrix $S_m^k(x,y)$, which is produced by the pixel-by-pixel movement of the matrix $S_m^k(x,y)$ over the random pattern. $S_m^k(0,0)$ denotes the center pixel of the selected window of the random pattern. Experimentally recorded SPs used in the evaluation process are 1000×1000 pixels. We have selected a window of size (x, y) = 300 × 300 pixels for estimation of the two-point correlation function, and the remaining 700 × 700 pixels are allocated for the 2D scanning of $S_m^k(x,y)$ over the random pattern for different realizations in the spatial averaging. Fig. 4.3(b) shows the correlation of fluctuation of these two SPs as calculated by Eq. (4.4), which indicates the presence of correlation fringes in the Stokes correlation. Fourier processing of this correlation fringes provides us with the desired BCP matrix. Fig. 4.3(c) shows the Fourier spectra of Fig. 4.3(b), where a marked red circle represents the information carried in arm 1 at the GG plane. A selected spectrum is brought back to the center, as shown in Fig. 4.3(d). An inverse Fourier transform operation on this spectrum (Fig. 4.3(d)) provides a complex

element of the BCP matrix, as shown in Fig. 4.3(e). This process is implemented to reconstruct all four elements of the BCP matrix.

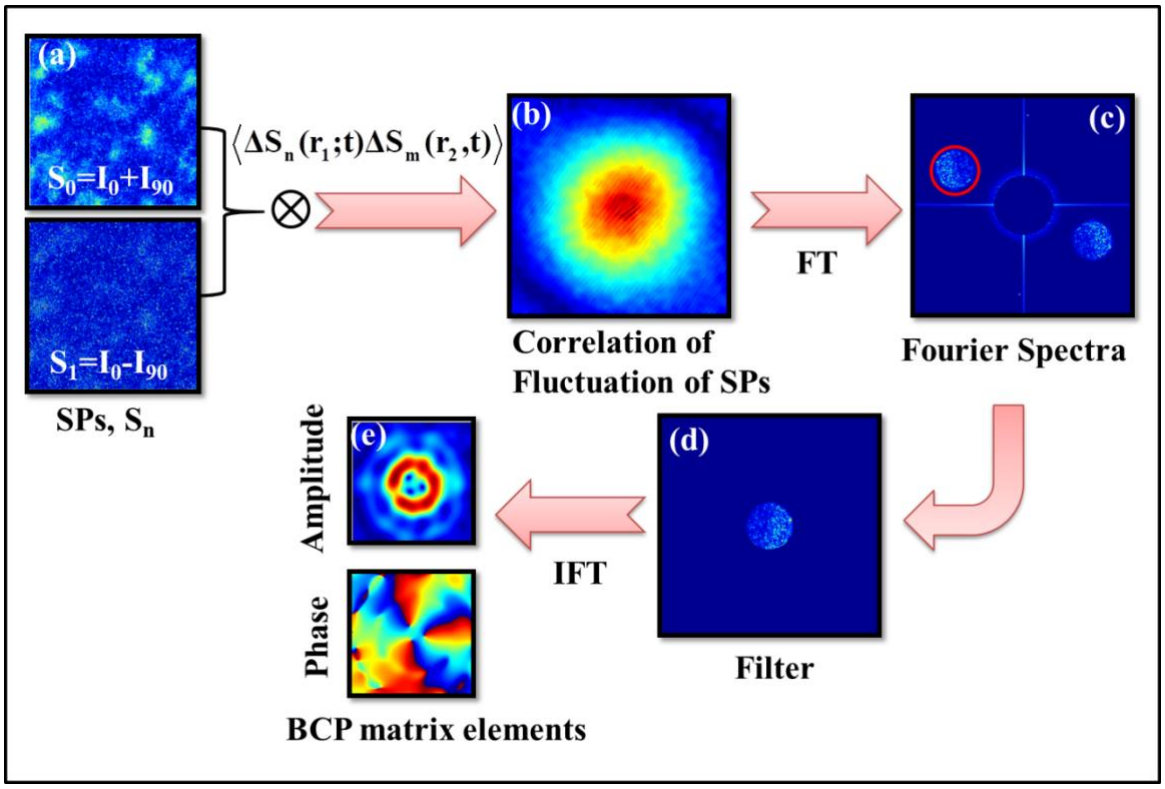

Fig. 4.3 Digital reconstruction of elements of the BCP matrix from the correlation of fluctuation of SPs. (a) experimentally measured SPs; (b) the correlation of fluctuation of SPs; (c) Fourier spectra of correlation of fluctuation of SPs; (d) In the Fourier spectra, central dc term is digitally suppressed to highlight the spectra and one spectrum is filtered out and shifted to the center (circled by a red circle); (e) reconstructed $W_{pq}^{1}(\Delta \boldsymbol{r})$; FT and IFT are Fourier transform and inverse Fourier transform operations, respectively.

The experimentally measured elements of the BCP matrix for the synthesized vector source is shown in Figs. 4.4. Figs. 4.4(a)-4.4(d) represents the amplitude distribution of the elements of the BCP matrix, i.e., $W_{xx}^{1}(\Delta \boldsymbol{r}), W_{xy}^{1}(\Delta \boldsymbol{r}), W_{yx}^{1}(\Delta \boldsymbol{r}), W_{yy}^{1}(\Delta \boldsymbol{r})$ for the vortex with *l*=3 and Figs. 4.4(e)-4.4(h) are the corresponding phase distribution. The vortex phase is introduced in x polarization component of the light by the SLM and beam size is 4 mm. Diagonal elements $W_{xx}^{1}(\Delta \boldsymbol{r})$ and $W_{yy}^{1}(\Delta \boldsymbol{r})$ of the BCP matrix are real, i.e., uniform

phase distribution as shown in Figs. 4.4(e), 4.4(h) while the off-diagonal elements $W_{xy}^{1}(\Delta \boldsymbol{r})$ and $W_{yx}^{1}(\Delta \boldsymbol{r})$ of the BCP matrix are complex as shown in Figs. 4.4(f), 4.4(g). The amplitude distributions in Figs. 4.4(b), 4.4(c) demonstrates the presence of a dark core encircled by a uniform intensity distribution and corresponding phase distributions show helical phase structures as shown in Figs. 4.4(f), 4.4(g). The formation of a doughnut structure with helical phase structure in the off-diagonal elements of the BCP matrix is associated with the complex nature of the source structure for $I_{pq}^{1}(\boldsymbol{\rho})$, where $p \neq q$.

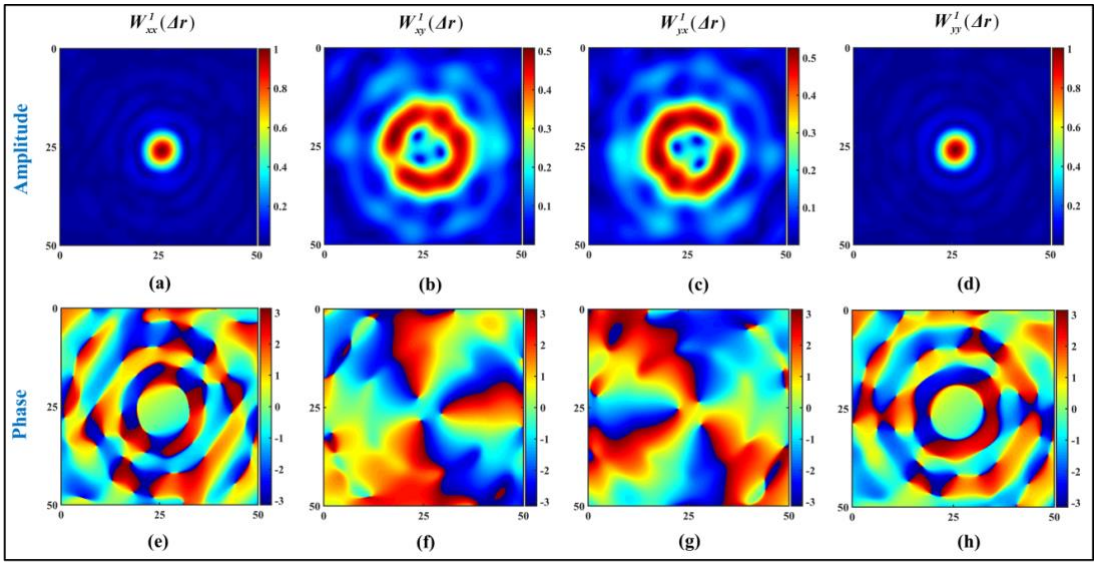

Fig. 4.4 Experimental results: (a)-(d) represent amplitude distribution of the elements of the BCP matrix for the vortex with *l*=3. (e)-(h) are the corresponding phase distribution.

4.4 Two-shot SPs to measure BCP matrix

The next goal of this chapter is to exploit the temporal correlations of a temporally fluctuating vector random field, which arises when a vector source passes through a dynamic diffuser to mimic the scattering environments containing fog or atmospheric turbulence. The folded interferometer makes the interference of temporally fluctuating vector source and a known reference and records the temporally fluctuating intensity

patterns to record a series of SPs, namely S_0 and S_1. Correlations of the fluctuations of these temporally fluctuating SPs are used to determine all four elements of the BCP matrix. The detailed analysis of the experimental setup and results for the measurement of the BCP matrix for temporally fluctuating fields are discussed below.

4.4.1 Experiment

To experimentally demonstrate the BCP matrix measurement for dynamic vector random fields, we implemented an experimental setup as shown in Fig. 4.5. Generation of the vector source is facilitated with a 45° linearly polarized beam incident on a phase-only SLM with a resolution of 1920 × 1080 and a pixel pitch of 8 μm (Pluto from Holoeye). The 45° linearly polarized beam is created using a He-Ne laser of wavelength 632.8 nm and a HWP. The horizontal polarization component of the beam carried the phase information loaded onto the SLM, while the vertical polarization component remained unaffected.

The modulated beam from the SLM was guided into a compact folded interferometer specifically designed for our experiment. This interferometer employs a cube BS to create a folded wavefront replica. The two resulting wavefronts serve distinct purposes: the first arm, arm 1, carries the encoded phase information from the SLM, while the second arm, arm 2, functions as a reference wave. In arm 2, the beam is focused at the center of the PA with the help of lens L1 of focal length, f=100 mm, creating a reference point source. The BS is oriented so that the two emerging replicas fall on two separate spatial regions of the rotating ground glass (RGG). The RGG generates an incoherent light source which is Fourier transformed by a lens L2 (f=200 mm) at the camera plane.

The generated random field at the camera plane follows Gaussian statistics. To experimentally measure all four elements of the BCP matrix, the filtered replica of arm 2 is Fourier transformed and used as a random reference field.

A CCD records a sequence of instantaneous intensity patterns composed of coherent superposition of random fields from arms 1 and 2. This CCD detector has a resolution of 1024 x 1392 pixels, a dynamic range of 14 bits, and a pixel pitch of 6.45 μm (pco.pixelfly USB). The RGG rotation speed is controlled to detect the series of instantaneous intensity patterns.

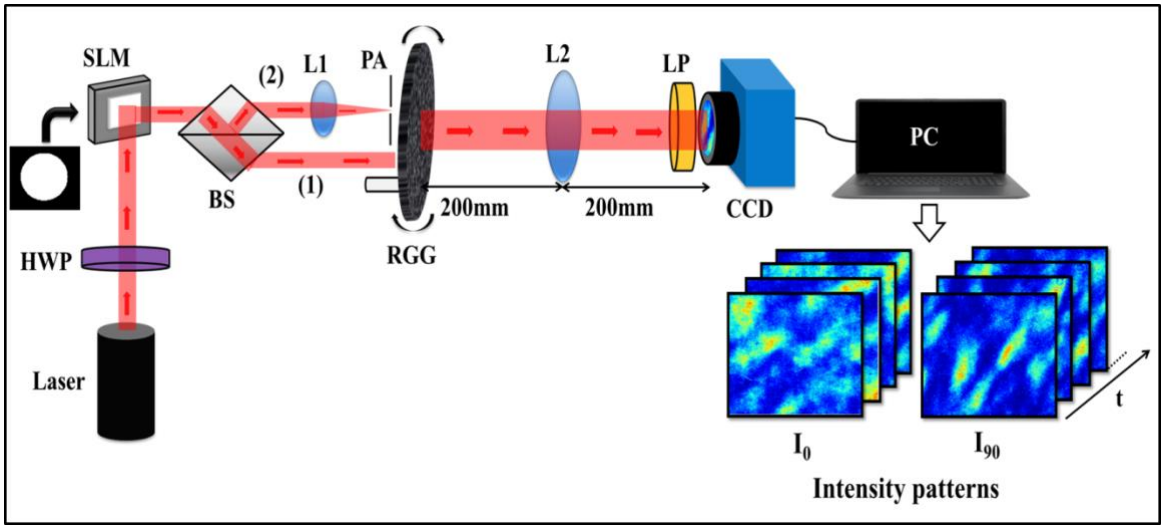

Fig. 4.5 Experimental implementation of the proposed technique. Laser: He-Ne laser, HWP: Half wave plate, SLM: Spatial light modulator, BS: Beam splitter, RGG: Rotating Ground Glass, L1, L2: Lenses, PA: Pinhole Aperture, LP: Linear polarizer, CCD: Charge-coupled device. Labels (1) and (2) denote arm 1 and arm 2, respectively.

The random field coming out of reference arm 2 is independent of the arm 1. This justifies the consideration of the fact that there is no correlation between fields coming from these two sources, i.e. $\left\langle U_p^{1*}(\boldsymbol{r}_1)U_q^2(\boldsymbol{r}_2)\right\rangle \approx 0$.

We inserted a LP before the CCD to measure the desired SPs and calculated two SPs using Eqs. (4.41-4.42). The correlation between fluctuations of SPs is digitally evaluated

from the experimentally measured SPs using averaging of a series of random patterns to replace the ensemble averaging for Gaussian statistics. This process provides $C_{00}(\Delta \boldsymbol{r}), C_{01}(\Delta \boldsymbol{r}), C_{10}(\Delta \boldsymbol{r}), C_{11}(\Delta \boldsymbol{r})$ from the experimental measured SPs and complex elements of the BCP matrix are retrieved as explained in Eqs. (4.4-4.31).

4.4.2 Experimental results and discussions

To experimentally demonstrate the proposed technique, we have synthesized two vector sources as presented in Table 4.1.

Vector Source	**Orthogonal field components**
Case 1	$U_x(\boldsymbol{\rho}) = 1, U_y(\boldsymbol{\rho}) = 1$
Case 2	$U_x(\boldsymbol{\rho}) = exp(il\varphi), U_y(\boldsymbol{\rho}) = 1$ where φ is the azimuthal phase, and l is the topological charge

Table 4.1 Description of different vector sources.

Experimentally recorded intensity patterns of the vector source (case 1 of Table 4.1) are used to evaluate $S_0(\boldsymbol{r}), S_1(\boldsymbol{r})$ from Eqs. (4.41), and (4.42), as shown in Fig. 4.6(a). From the experimentally measured SPs, digital evaluations of correlations of fluctuations of the SPs are acquired by spatial averaging. This process is executed by taking the SPs as a matrix, $S_m(\boldsymbol{r})$ where m = 0, 1, denotes the two SPs involved in the estimation of polarization correlation, and, $\boldsymbol{r} = (x, y)$ is the pixel spatial coordinate which takes values up to 1000 × 1000 pixels. In the next step, we execute the two-point correlations of SPs

fluctuations, $\Delta S_m^j(\boldsymbol{r_1})\Delta S_m^j(\boldsymbol{r_2})$ for different realizations of the random fields, and this process is represented as $\sum_{j=1}^{600}\left[\Delta S_m^j(\boldsymbol{r_1})\Delta S_m^j(\boldsymbol{r_2})\right]$, where, j represents each realization of the random intensity patterns, which ranges from 1 to 600 in our experiment. Fig. 4.6(b) shows the correlation of fluctuation of the SPs as calculated by Eq. (4.4). Fig. 4.6(c) shows the Fourier spectra of Fig. 4.6(b), where a marked red circle represents the information carried in arm 1 at the RGG plane. A selected spectrum is brought back to the center, as shown in Fig. 4.6(d). An inverse Fourier transform operation on this spectrum (Fig. 4.6(d)) provides a complex element of the BCP matrix, as shown in Fig. 4.6(e). This process is implemented to reconstruct all four elements of the BCP matrix. The experimentally measured elements of the BCP matrix for two different cases, as presented in Table 4.1, are shown in Figs. 4.7 and 4.8. Figs. 4.7(a)-4.7(d) represents the amplitude distribution of the elements of the BCP matrix, i.e., $W_{xx}^1(\Delta\boldsymbol{r}), W_{xy}^1(\Delta\boldsymbol{r}), W_{yx}^1(\Delta\boldsymbol{r}), W_{yy}^1(\Delta\boldsymbol{r})$ for the vector source (case 1) and Figs. 4.7(e)-4.7(h) are the corresponding phase distributions. Figs. 4.7(e)-(h) show nearly uniform phase values and these results appear due to a circular symmetric source of diameter 4mm at the RGG plane, as presented in Table 4.1. The physical basis of these structures, shown in Figs. 4.7, can be explained using the vectorial vCZ theorem [211] and using Eq. (4.38).

On the other hand, Figs. 4.8(a)-4.8(d) represent the amplitude distribution of the elements of the BCP matrix, i.e., $W_{xx}^1(\Delta\boldsymbol{r}), W_{xy}^1(\Delta\boldsymbol{r}), W_{yx}^1(\Delta\boldsymbol{r}), W_{yy}^1(\Delta\boldsymbol{r})$ for the second case, and Figs. 4.8(e)-4.8(h) are the corresponding phase distribution. The vortex phase with l=1 is introduced in the x polarization component of the light by the SLM, and the beam size is 4 mm. Diagonal elements of the BCP matrix are real, i.e., uniform phase distribution, as shown in Figs. 4.8(e), 4.8(h), while the off-diagonal elements of the BCP matrix are

complex, as shown in Figs. 4.8(f), 4.8(g). The amplitude distributions in Figs. 4.8(b), 4.8(c) demonstrate the presence of a dark core encircled by a uniform intensity distribution and corresponding phase distributions show helical phase structures as shown in Figs. 4.8(f), 4.8(g). The formation of a doughnut structure with helical phase structure in the off-diagonal elements of the BCP matrix is associated with the complex nature of the source structure for $I_{pq}^{1}(\boldsymbol{\rho})$, where $p \neq q$.

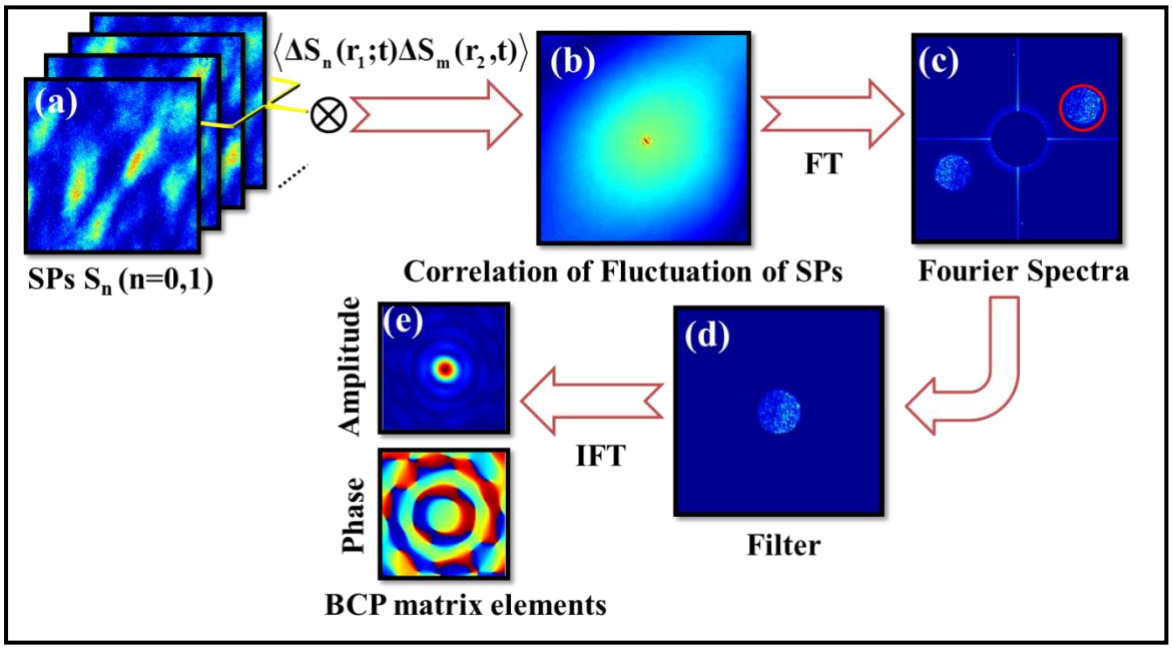

Fig. 4.6 Digital reconstruction of elements of the BCP matrix from the correlation of fluctuation of SPs. (a) experimentally measured SPs; (b) the correlation of fluctuation of SPs; (c) Fourier spectra of correlation of fluctuation of SPs; (d) In the Fourier spectra, central DC term is digitally suppressed to highlight the spectra and one spectrum is filtered out and shifted to the center (circled by a red circle); (e) reconstructed $W_{pq}^{1}(\Delta \boldsymbol{r})$; FT and IFT are Fourier transform and inverse Fourier transform operations, respectively.

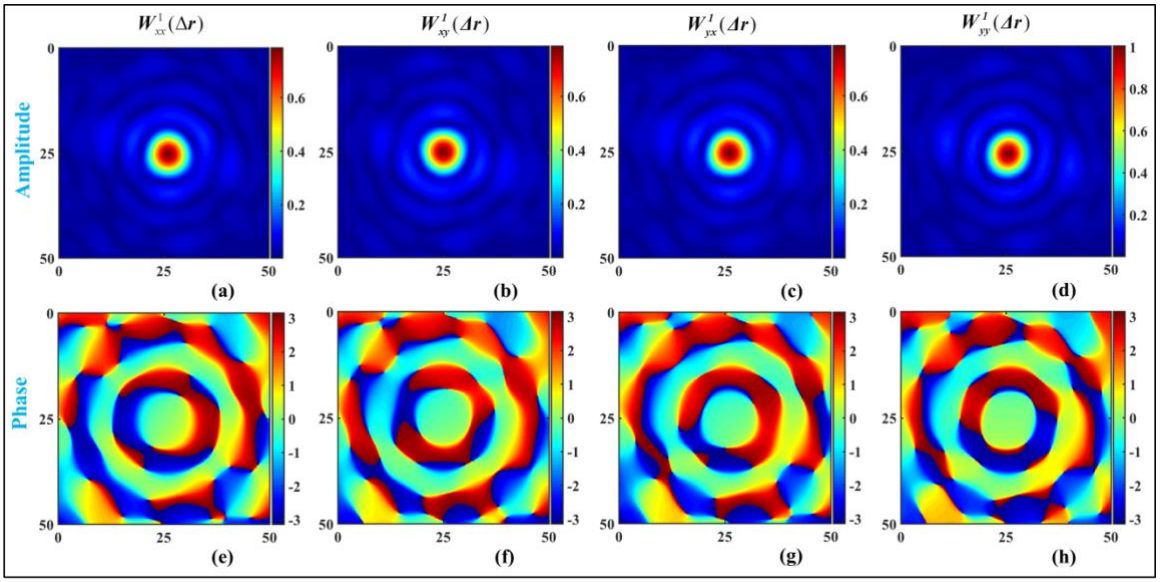

Fig. 4.7 Experimental results: (a)-(d) represent amplitude distribution of the elements of the BCP matrix for the circular aperture of diameter 4mm. (e)-(h) are the corresponding phase distribution.

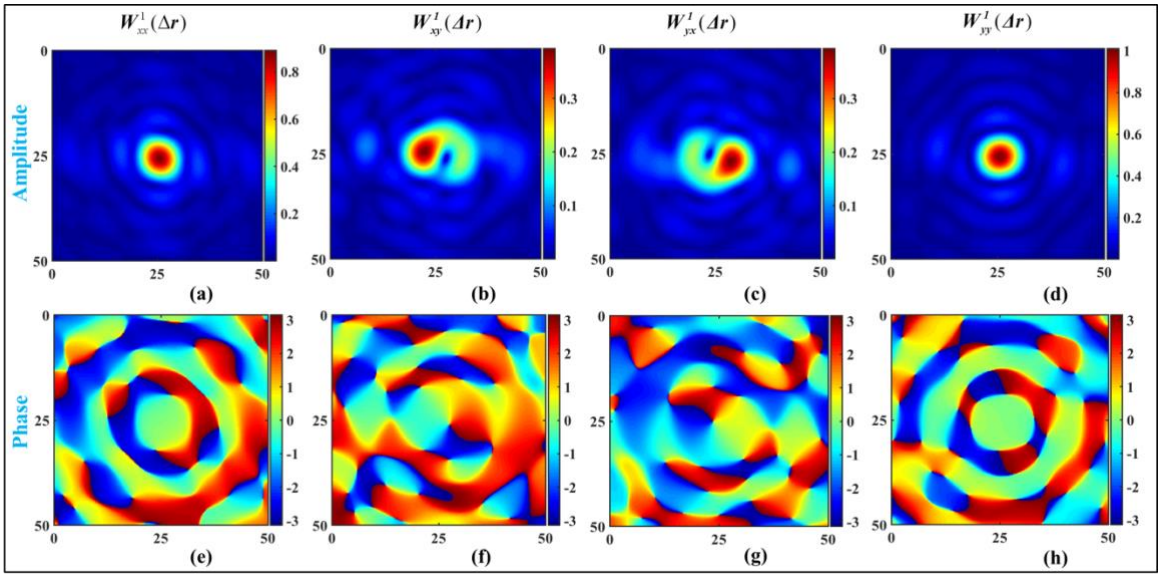

Fig. 4.8 Experimental results: (a)-(d) represent amplitude distribution of the elements of the BCP matrix for the vortex with l=1. (e)-(h) are the corresponding phase distribution.

The reconstruction quality of the BCP matrix in this experimental design depends on the number of recorded intensity patterns, reference beam spot, size of optics, and a leakage in the orthogonal polarization components.

4.5 Single-shot SPs to measure BCP matrix

In the next work, we demonstrate a new technique for experimental measurement of all four elements of the BCP matrix of spatially fluctuating vector random field from a single intensity pattern. This intensity pattern measures the two SPs, namely $S_0(\boldsymbol{r})$ and $S_1(\boldsymbol{r})$, from a single-frame intensity recording and uses these parameters to extract the BCP matrix. Measurement of the desired SPs, $S_0(\boldsymbol{r})$ and $S_1(\boldsymbol{r})$ requires the intensities of orthogonally polarized components of vector field. A commercially available Wollaston prism or beam displacer can separate the orthogonally polarized components of the vector field; however, due to the propagation of light through the scatterer and high-angle scattering, it is hard to isolate the vector random patterns of the orthogonal polarization components at the recording plane by a fixed angle Wollaston prism or beam displacer. To make this possible, we devised a tuneable beam displacer and realized the measurement of two SPs, $S_0(\boldsymbol{r})$ and $S_1(\boldsymbol{r})$, in a single frame. Hence, this scheme is free from a mechanical rotation of quarter-wave plate and linear polarizer, usually required to measure SPs. The experimental implementation of our technique consists of two parts. In the first part, we employed a folded interferometer that effectively facilitated the interference of a field to be analyzed with a reference field for BCP matrix measurement in the Stokes correlations. The second part tackles the issue of multiple measurements for the desired SPs by incorporating a tuneable beam displacer in the experiment. This beam displacer captures the orthogonal polarization components in a single recording and measures $S_0(\boldsymbol{r})$ and $S_1(\boldsymbol{r})$ from a single shot. Subsequently, correlations of the fluctuations of these two SPs are used to measure all four elements of the BCP matrix. Our approach demonstrates the feasibility of using fewer measurements to measure two-point correlations of vector fields. Detailed theoretical framework and experimental results are discussed below.

4.5.1 Experiment

To experimentally validate the proposed technique, we designed a highly compact folded interferometric geometry along with a tuneable beam displacer, as shown in Fig.1. The experimental setup depicted in Fig. 4.9(a) comprises two principal sections: Part I, which involves a source synthesis unit and an experimental arrangement to realize a coherent superposition of the unknown vector source, i.e., the field to-be-analyzed, and a reference vector field. Part II is dedicated to recording orthogonal polarization components in a single frame. A detailed explanation of our experimental methodology is explained below.

Part I: A spatially filtered, vertically polarized beam from a He-Ne laser (Thorlabs, HNL150L) with a wavelength of 632.8 nm is transformed into a 45^0 linearly polarized beam by a HWP oriented at 22.5^o with respect to the vertical direction. This beam is directed on the phase-only SLM with a 1920 × 1080 pixels resolution and a pixel pitch of 8 μm (Pluto, Holoeye). The SLM encodes information in the horizontal polarization component, leaving the vertical component unaltered. This beam proceeds to a compact and folded interferometer. It utilizes a reversed wavefront configuration to make an interference of a vector source and reference in a nearly common path configuration. Two emerging replicas from the BS, denoted by arm 1 and arm 2, are used to realize a compact folded interferometer. Arm 1 carries the complex information encoded by SLM, and arm 2 is a reference. A replica in arm 2 is focused at the center of the PA through a lens L1 of a focal length of 100 mm to generate a reference point source.

These two replicas illuminate separate spatial regions of a GG. Light beams scatter from the GG and generate two statistically independent random fields; one corresponds to the field to be analyzed and is referred to as ‘1’. Second is a reference random field, referred

as '2'. Subsequently, these two random fields are Fourier transformed by a lens L2 of focal length 200 mm. A coherent summation of these fields is recorded by a CCD placed at the back focal plane of lens L2.

Part II: A specially designed polarization-sensitive triangular Sagnac geometry is utilized with adjustable separation of the orthogonally polarized intensity patterns. The Sagnac geometry consists of two mirrors (M1 and M2) and a polarizing beam splitter (PBS). A horizontal polarization component transmits through the PBS, and a vertical polarization component reflects through the PBS. The two counter-propagating orthogonally polarized beams travel nearly equal paths and are directed by M1 and M2 toward the CCD plane through the PBS. This experimental configuration enables the creation of images of the orthogonally polarized intensity patterns at the CCD plane with the help of a lens L3 positioned in a 2*f* configuration with *f*=200mm. The CCD camera has a resolution of 1392 × 1040 pixels and a pixel size of 6.45μm (pco.pixelfly usb). The spatial separation of the orthogonal polarization components is adjusted via mirrors M1 and M2 within the Sagnac setup, allowing for the independent recording of the orthogonally polarized intensity components in a single-frame. A laboratory picture of the experimental setup is shown in Fig. 4.9(b).

4.5.2 Experimental results and discussions

To experimentally test the proposed technique, we have demonstrated the single-shot measurement of the BCP matrix for the three experimentally synthesized vector sources in the far-field, as presented in Table 4.2.

Vector Source	**Orthogonal field components**
Case 1	$U_x(\boldsymbol{\rho}) = 1, U_y(\boldsymbol{\rho}) = 1$
Case 2	$U_x(\boldsymbol{\rho}) = exp(il\varphi), U_y(\boldsymbol{\rho}) = 1$ where φ is the azimuthal phase, and l is the topological charge
Case 3	$U_x(\boldsymbol{\rho}) = exp(ia\boldsymbol{\rho}), U_y(\boldsymbol{\rho}) = 1$ where, a is the axicon parameter.

Table 4.2 Different vector sources used in this technique.

Fig. 4.10 highlights a flow chart describing the digital reconstruction steps used in the measurement of elements of the BCP matrix. The experimentally recorded single-frame intensity pattern for the vector source (case 2 of Table 4.2) is shown in Fig. 4.10(a). The left and right panels in Fig. 4.10(a) represent the intensities of the horizontal and vertical polarization components. These two intensity patterns are utilized to evaluate $S_0(\boldsymbol{r})$ and $S_1(\boldsymbol{r})$, and results are shown in Fig. 4.10(b) and 4.10(c), respectively. From the experimentally measured SPs, digital evaluations of correlations of fluctuations of the SPs are acquired by spatial averaging. This process is executed like the steps as described in section 4.3.2. Experimentally recorded SPs used in the evaluation process are 670×670 pixels. We have selected a window of size (x, y) = 200 × 200 pixels to estimate the two-point correlation function. The remaining 470 × 470 pixels are allocated for the 2D scanning of SPs over the random pattern for different realizations in the spatial averaging.

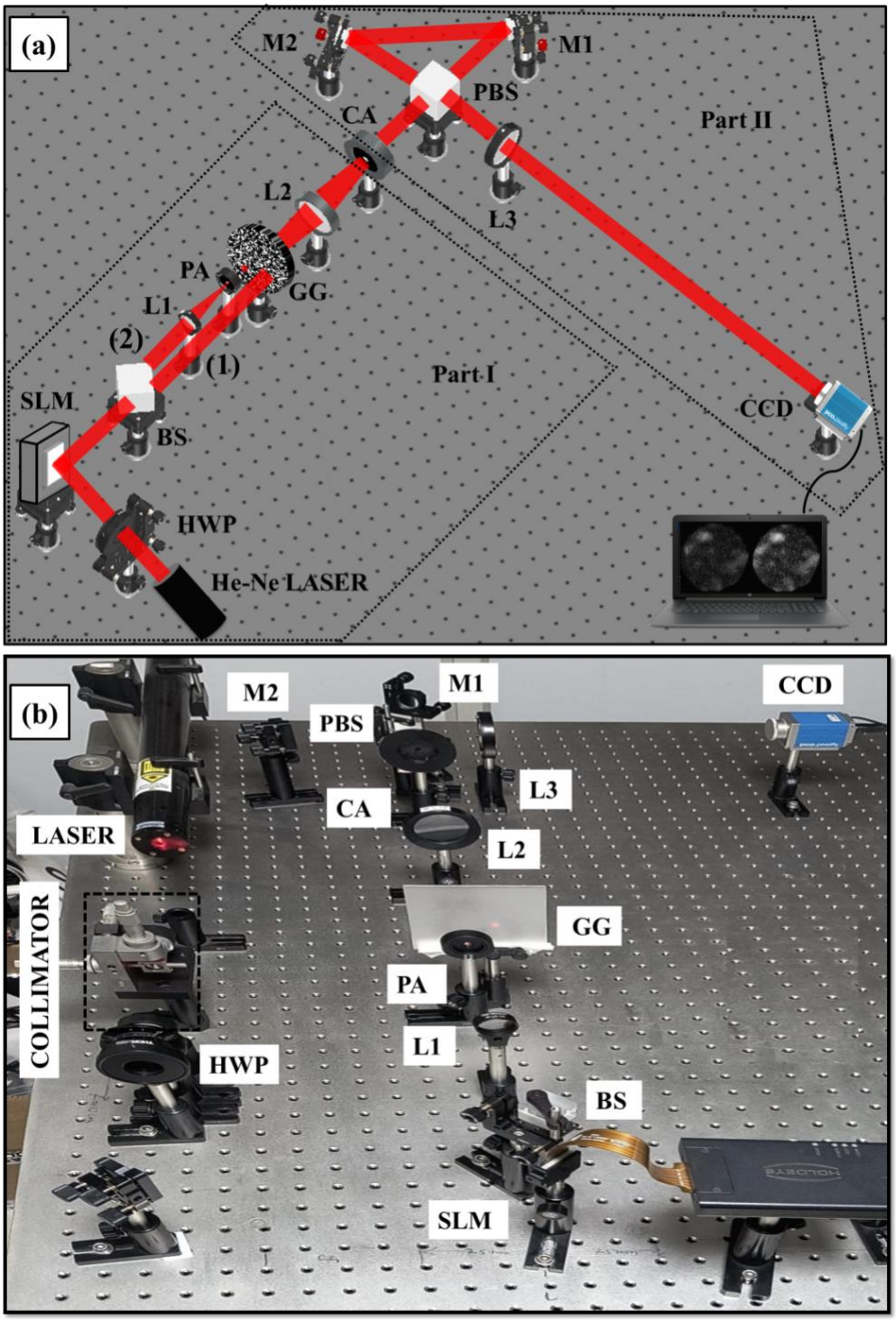

Fig. 4.9 (a) Experimental setup. Laser: He-Ne laser, HWP: Half wave plate, SLM: Spatial light modulator, BS: Beam splitter, GG: Ground Glass, L1, L2, L3: Lenses, PA: Pinhole Aperture, CA: Circular Aperture, PBS: Polarizing Beam splitter, M1, M2: Mirrors, CCD: Charge-coupled device. Labels (1) and (2) denote arm 1 and arm 2, respectively. (b) Laboratory picture of the experimental setup.

The correlation of fluctuation of the SPs provides $C_{00}(\Delta \boldsymbol{r}), C_{01}(\Delta \boldsymbol{r}), C_{10}(\Delta \boldsymbol{r}), C_{11}(\Delta \boldsymbol{r})$ which are used to measure the modulus square of the elements of the BCP matrix, i.e. $\left|W_{pq}(\Delta \boldsymbol{r})\right|^2$ as explained in Eqs. (4.6-4.31) and one of the modulus squares of the elements of the BCP matrix, i.e., $\left|W_{xy}(\Delta \boldsymbol{r})\right|^2$ for the vortex structure, is shown in Fig. 4.10(d). Fig. 4.10(e) showcases the Fourier spectra of Fig. 4.10(d), where a marked green circle indicates the information loaded into arm 1 at the GG plane. A selected spectrum is brought back to the center as shown in Fig. 4.10(f), and the inverse Fourier transform of the centered spectrum yields the complex element of the BCP matrix. Results are shown in Fig. 4.10(g) and 4.10(h) for amplitude and phase respectively. This process is adopted to reconstruct all four elements of the BCP matrix. Different combinations of $C_{00}(\Delta \boldsymbol{r}), C_{01}(\Delta \boldsymbol{r}), C_{10}(\Delta \boldsymbol{r}), C_{11}(\Delta \boldsymbol{r})$ are used to calculate $\left|W_{pq}(\Delta \boldsymbol{r})\right|^2$ for the three vector sources, which are shown in Fig. 4.11. Fourier processing of $\left|W_{pq}(\Delta \boldsymbol{r})\right|^2$ as explained in Eq. (4.32) and as depicted in Fig. 4.10 is performed to determine all four elements of the BCP matrix for the three vector sources. Repeating the Fourier processing as outlined in Eq. (4.32) and as shown in Figs. 4.10(e)–4.10(h), amplitude and phase distributions of the elements of the BCP matrix for the three vector sources are obtained, and the results are presented in Figs. 4.12–4.14.

The first row in Fig. 4.12(a)-(d) represents the amplitude distribution of the elements of the BCP matrix for the vector source (case 1) of diameter 4 mm at the GG plane. The second row in Fig 4.12 presents the corresponding phase distributions. All the elements of the BCP matrix in Fig. 4.12 are real with zero-phase values. A zero-phase value in Figs. 4.12(e)–(h) for a circular symmetric vector source agrees with the analytical results based on the vectorial vCZ theorem and Eq. (4.38).

On the other hand, Figs. 4.13(a)-(d) in the first row represent the amplitude distribution of the elements of the BCP matrix for case 2, and corresponding phase distributions are shown in Fig. 4.13(e)-(h). The SLM inserts the vortex phase in the x-polarization component of the beam, and the source diameter is 4 mm. The first and fourth columns in Fig. 4.13 show the amplitude and phase distributions of the diagonal elements $W_{xx}^{1}(\Delta \boldsymbol{r})$ and $W_{yy}^{1}(\Delta \boldsymbol{r})$ of the BCP matrix, respectively, which are real and without phase variation. The second and third columns in Fig. 4.13 present the amplitude and phase distributions of the off-diagonal elements $W_{xy}^{1}(\Delta \boldsymbol{r})$ and $W_{yx}^{1}(\Delta \boldsymbol{r})$ of the BCP matrix, respectively, which are complex. The amplitude distributions in Figs. 4.13(b), 4.13(c) reveals a "doughnut"-shaped structure, and corresponding phase distributions show a helical phase structure as shown in Figs. 4.10(f), 4.10(g). The formation of the doughnut structure with a helical phase structure in the off-diagonal elements of the BCP matrix is attributed to the complex nature of the source $I_{pq}^{1}(\boldsymbol{\rho})$, where $p \neq q$.

Moreover, the first row in Fig. 4.14 represents the amplitude distribution of the elements of the BCP matrix for case 3, and corresponding phase distributions are shown in the second row of Fig. 4.14. The axicon phase is inserted in the x polarization component of the light by the SLM, and the beam diameter is 4 mm. Similar to the previous case, diagonal elements $W_{xx}^{1}(\Delta \boldsymbol{r})$ and $W_{yy}^{1}(\Delta \boldsymbol{r})$ of the BCP matrix,–in the first and fourth columns of Fig. 4.14, are real with zero phases. In contrast, the off-diagonal elements $W_{xy}^{1}(\Delta \boldsymbol{r})$ and $W_{yx}^{1}(\Delta \boldsymbol{r})$ of the matrix, as shown in the second and third columns of Fig. 4.14, are complex. A Bessel function distribution in the off-diagonal elements of the BCP matrix is associated with the axicon structure inserted at the source as for $I_{pq}^{1}(\boldsymbol{\rho})$, where $p \neq q$.

The developed theoretical basis of SPs correlation for complete recovery of the BCP matrix in one shot can also be realized using alternative experimental geometries and for temporally fluctuating fields. The effectiveness of reconstructing the BCP matrix in the experiment depends on several factors, such as optics size, reference coherence, speckle size at the detector, and the response of optics in polarization selection etc.

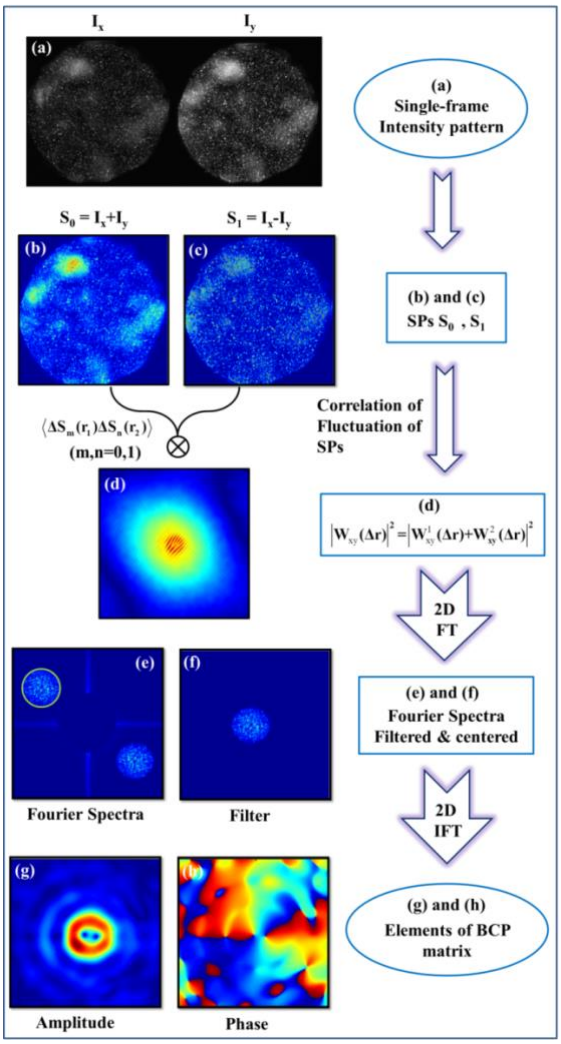

Fig. 4.10 Digital reconstruction process of elements of the BCP matrix from the correlation of fluctuations of the SPs. (a) single-frame intensity recording; (b), (c) calculated SPs from (a); (d) $\left|W_{pq}(\Delta \boldsymbol{r})\right|^2$ acquired from the correlation of fluctuation of SPs and represents fringes as indicated in the insets; (e) Fourier spectra of $\left|W_{pq}(\Delta \boldsymbol{r})\right|^2$ (f) Selected and centered Fourier spectra (marked by a circle); (g), (h) reconstructed $W^1_{pq}(\Delta \boldsymbol{r})$; FT and IFT are Fourier transform and inverse Fourier transform operations, respectively.

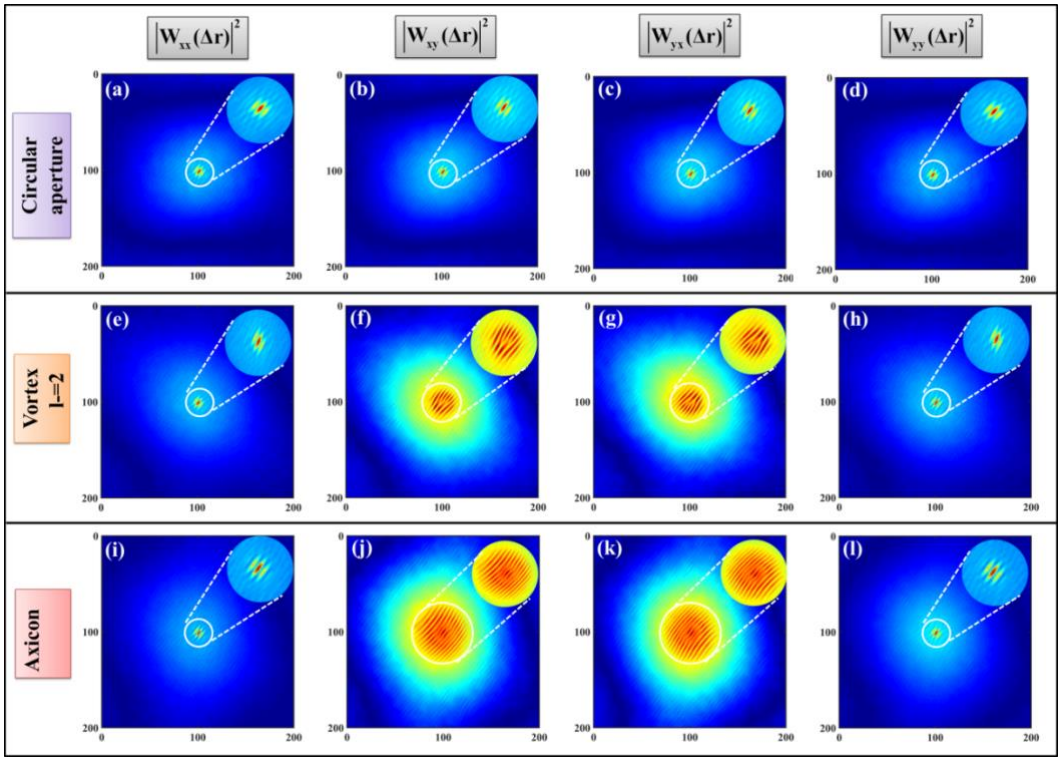

Fig. 4.11 Modulus square of the elements of the BCP matrix of the coherent summation of vector sources and reference random field at the detector plane. Results in the first row in Figs (a)-(d) correspond to case 1; the second row in Figs. (e)-(h) present results correspond to case 2; third row in Figs. (i)-(l) present results correspond to case 3.

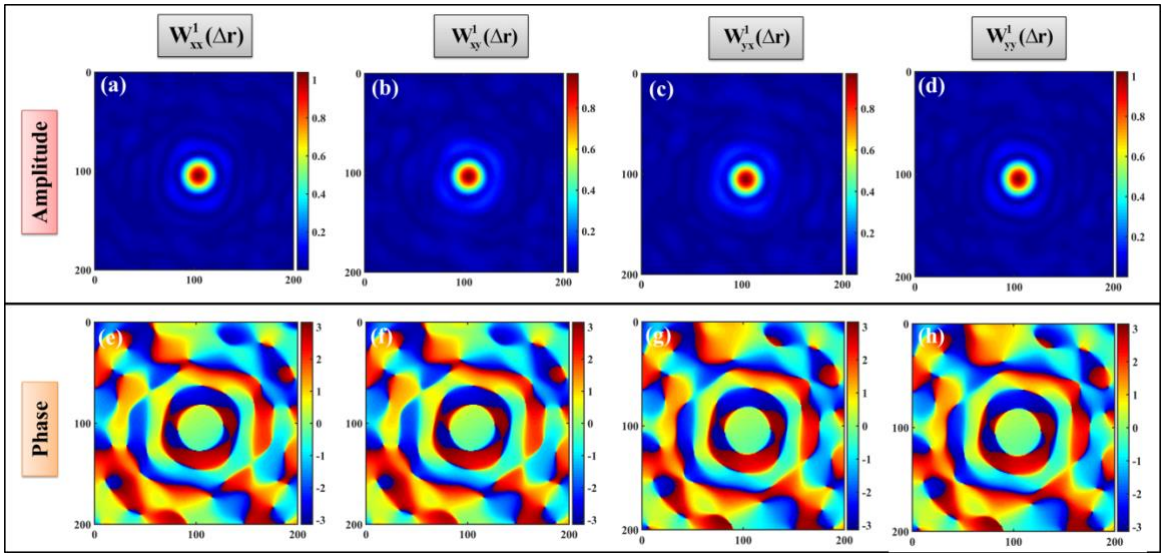

Fig. 4.12 Experimentally recovered complex elements of the BCP matrix for case 1 with circular aperture of diameter 4mm; (a)-(d) represents the amplitude distribution of the elements of the BCP matrix; (e)-(h) are the corresponding phase distributions**.**

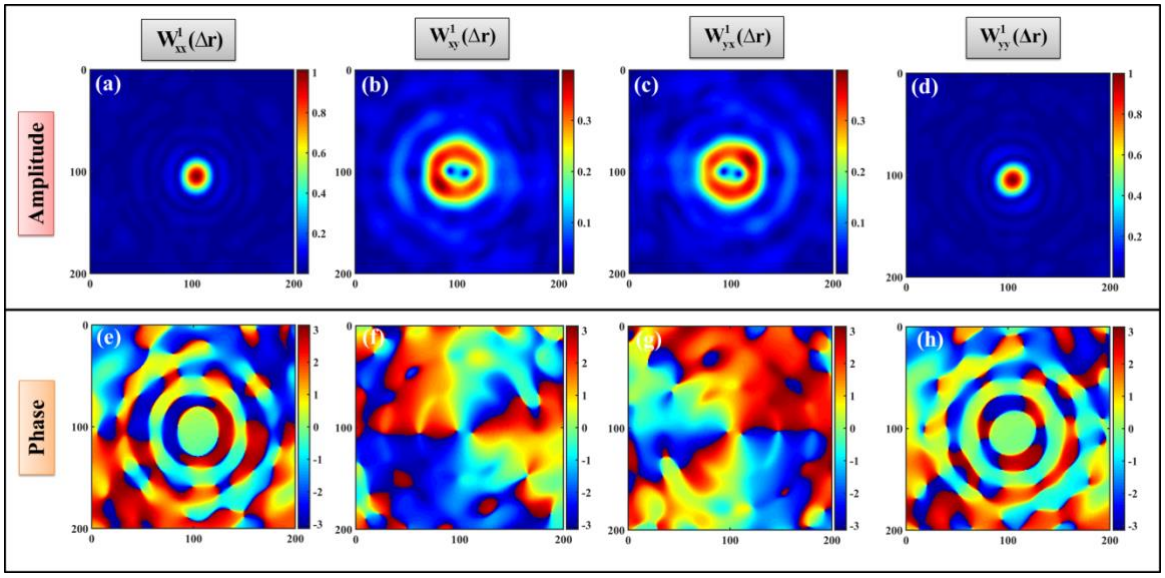

Fig. 4.13 Experimentally recovered complex elements of the BCP matrix for case 2 with *l*=2. (a)-(d) represents the amplitude distribution of the elements of the BCP matrix; (e)-(h) are the corresponding phase distributions.

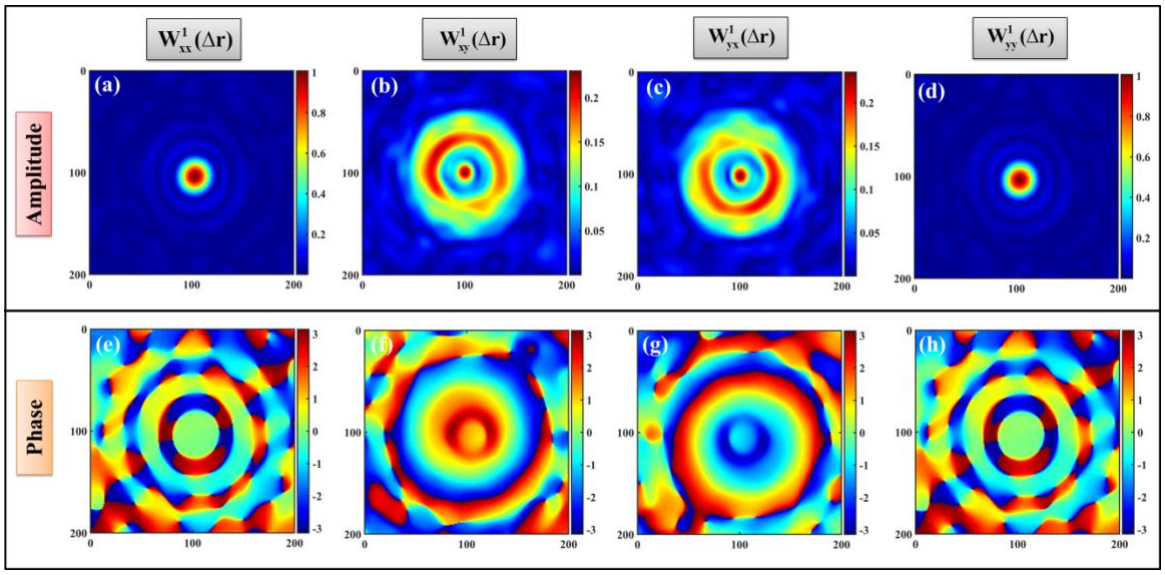

Fig. 4.14 Experimentally recovered complex elements of the BCP matrix for case 3 with axicon function. (a)-(d) represents the amplitude distribution of the elements of the BCP matrix; (e)-(h) are the corresponding phase distribution.

4.6 Conclusions

In this chapter, we have presented three new experimental techniques for quantitatively measuring all four elements of the BCP matrix for spatially and temporally fluctuating

vector fields. The theoretical basis of the proposed method is established within the framework of the correlations of fluctuations of the only two SPs, namely $S_0(\boldsymbol{r})$ and $S_1(\boldsymbol{r})$ and verified by experimental tests.

A compact, stable folded interferometer is designed for the interference of a field to-be-analyzed with a reference field to extract the complex elements of BCP matrix in the developed Stokes correlation approach. In the first two experiments, the SPs are measured by inserting a LP before the CCD and BCP matrix measurements are performed for both spatially and temporally fluctuating intensity patterns.

In the third technique, we coupled our specially designed folded interferometer with a tuneable beam displacer for the single-shot measurement of the desired two SPs, $S_0(\boldsymbol{r})$ and $S_1(\boldsymbol{r})$. Experimental results for different vector sources are presented in each technique, demonstrating our techniques' feasibility. Fourier processing of two SPs fluctuation correlation enables the extraction of all four elements of the BCP matrix. These techniques are expected to play a crucial role in polarization imaging through random media, characterizing polarization dynamics of random electromagnetic fields, coherence analysis, and looking through randomness.